

Source–detector calibration in three-dimensional Bayesian optical diffusion tomography

Seungseok Oh and Adam B. Milstein

School of Electrical and Computer Engineering, Purdue University, West Lafayette, Indiana 47907-1285

R. P. Millane

Department of Electrical and Computer Engineering, University of Canterbury, Private Bag 4800, Christchurch, New Zealand

Charles A. Bouman and Kevin J. Webb

School of Electrical and Computer Engineering, Purdue University, West Lafayette, Indiana 47907-1285

Received January 18, 2002; revised manuscript received May 16, 2002; accepted May 16, 2002

Optical diffusion tomography is a method for reconstructing three-dimensional optical properties from light that passes through a highly scattering medium. Computing reconstructions from such data requires the solution of a nonlinear inverse problem. The situation is further complicated by the fact that while reconstruction algorithms typically assume exact knowledge of the optical source and detector coupling coefficients, these coupling coefficients are generally not available in practical measurement systems. A new method for estimating these unknown coupling coefficients in the three-dimensional reconstruction process is described. The joint problem of coefficient estimation and three-dimensional reconstruction is formulated in a Bayesian framework, and the resulting estimates are computed by using a variation of iterative coordinate descent optimization that is adapted for this problem. Simulations show that this approach is an accurate and efficient method for simultaneous reconstruction of absorption and diffusion coefficients as well as the coupling coefficients. A simple experimental result validates the approach. © 2002 Optical Society of America

OCIS codes: 100.3010, 100.3190, 100.6890, 170.5280.

1. INTRODUCTION

Optical diffusion tomography is an imaging modality that has potential in applications such as medical imaging, environmental sensing, and nondestructive testing.¹ In this technique, measurements of the light that propagates through a highly scattering medium are used to reconstruct the absorption and/or the scattering properties of the medium as a function of position. In highly scattering media such as tissue, the diffusion approximation to the transport equation is sufficiently accurate and provides a computationally tractable forward model. However, the inverse problem of reconstructing the absorption and/or the scattering coefficients from measurements of the scattered light is highly nonlinear. This nonlinear inverse problem can be very computationally expensive, so methods that reduce the computational burden are of critical importance.^{2–6}

An important issue for practical optical diffusion imaging that is addressed in this paper is accurate modeling of the source and detector coupling coefficients.⁷ These coupling coefficients determine weights for sources and detectors in a diffusion equation model for the scattering domain. The physical source of the source–detector coupling variability is associated with the optical components external to the scattering domain: the placement of fibers, the variability in switches, etc. Variations in the coupling coefficients can result in severe, systematic

reconstruction distortions. In spite of its practical importance, this issue has received little attention.

Two preprocessing methods have been investigated to correct for source–detector coupling errors before inversion. Jiang *et al.*^{8,9} calibrated coupling coefficients and a boundary coefficient by comparing prior measurements of photon flux for a homogeneous medium with the corresponding computed values. This scheme has been applied in clinical studies.^{10–12} This method of calibration requires a set of reference measurements from a homogeneous sample, in addition to the measurements used to reconstruct the inhomogeneous image. Iftimia and Jiang¹³ proposed a preprocessing scheme that involved minimization of the mean square error between the measurements for the given inhomogeneous phantom and the computed values with an assumed homogeneous medium. However, although this approach does not require prior homogeneous reference measurements, it neglects the influence of an inhomogeneous domain in determining the source and detector weights.

In order to reconstruct the image from a single set of measurements from the domain to be imaged, it is necessary to estimate the coupling coefficients as the image is reconstructed. For example, Boas *et al.*⁷ proposed a scheme for estimating individual coupling coefficients as part of the reconstruction process. They simultaneously estimated both absorption and coupling coefficients by

formulating a linear system that consisted of the perturbations of the measurements in a Rytov approximation and the logarithms of the source and detector coupling coefficients. To our knowledge, no results have been reported for nonlinear reconstruction of both absorption and diffusion images and the individual coupling coefficients.

In this paper we describe an efficient algorithm for estimating individual source and detector coupling coefficients as part of the reconstruction process for both absorption and diffusion images. This approach is based on the formulation of our problem in a unified Bayesian regularization framework containing terms for both the unknown three-dimensional (3-D) optical properties and the coupling coefficients. The resulting cost function is then jointly minimized to both reconstruct the image and estimate the needed coefficients. To perform this minimization, we adapt our iterative coordinate decent optimization method² to include closed-form steps for the update of the coupling coefficient estimates. This unified optimization approach results in an algorithm that can reconstruct images and estimate the coupling coefficients without the need for prior calibration. In a previous experiment, we used the algorithm to effectively estimate a single coefficient from a measured 3-D data set.¹⁴ Simulation results show that our method can substantially improve reconstruction quality even when there are a large number of severely nonuniform coupling coefficients. Our approach is applied to a simple phantom experiment.

2. PROBLEM FORMULATION

In a highly scattering medium with low absorption, such as soft tissue in the 650–1300 nm wavelength range, the photon flux is accurately modeled by the diffusion equation.^{15,16} In frequency-domain optical diffusion imaging, the light source is amplitude modulated at angular frequency ω , and the complex modulation envelope of the photon flux is measured at the detectors. The complex amplitude $\phi_k(r)$ of the modulation envelope due to a point source at position a_k satisfies the frequency-domain diffusion equation

$$\nabla \cdot [D(r)\nabla \phi_k(r)] + [-\mu_a(r) - j\omega/c]\phi_k(r) = -\delta(r - a_k), \quad (1)$$

where r is position, c is the speed of light in the medium, $D(r)$ is the diffusion coefficient, and $\mu_a(r)$ is the absorption coefficient. We consider a region to be imaged that is surrounded by K point sources at positions a_k , for $1 \leq k \leq K$, and M detectors at positions b_m , for $1 \leq m \leq M$. The 3-D domain is discretized into N grid points, denoted by r_1, \dots, r_N . The unknown image is then represented by a $2N$ -dimensional column vector x containing the absorption and diffusion coefficients at each discrete grid point:

$$x = [\mu_a(r_1), \dots, \mu_a(r_N), D(r_1), \dots, D(r_N)]^T. \quad (2)$$

We use the notation $\phi_k(r; x)$ in place of $\phi_k(r)$ to emphasize the dependence of the solution to Eq. (1) on the unknown material properties x .

Let y_{km} be the complex measurement at detector location b_m and using a source at location a_k . This measurement is a sample of a random variable Y_{km} , which we will model as a sum of the true signal and Gaussian noise. The datum mean value of Y_{km} is given by

$$E[Y_{km}|x, s_k, d_m] = s_k d_m \phi_k(b_m; x), \quad (3)$$

where $\phi_k(b_m; x)$ is the solution of Eq. (1) evaluated at position b_m ; s_k and d_m are complex constants representing the unknown source and detector coupling coefficients; and $E[\cdot | x, s_k, d_m]$ denotes the conditional expectation given x , s_k , and d_m . (We assume that the physical sources and detectors provide an adequate measure of ϕ , that they do not perturb the diffusion equation solution, and that they have an equivalent point representation.)

Our objective is to simultaneously estimate the unknown image x together with the unknown source and detector coupling coefficient vectors $s = [s_1, s_2, \dots, s_K]^T$ and $d = [d_1, d_2, \dots, d_M]^T$. The coupling coefficients are different for different sources and detectors and are not known *a priori*. In general, the values of s_k and d_m will vary in both amplitude and phase for real physical systems. Typically, amplitude variations can be caused by different excitation intensities for the sources and different collection efficiencies for the detectors, and phase variation can be caused by the different effective positions of the sources and detectors. Without these parameter vectors, accurate reconstruction of x is not possible.

The measurement vector y is formed by raster ordering the measurements y_{km} in the form

$$y = [y_{11}, \dots, y_{1M}, y_{21}, \dots, y_{2M}, \dots, y_{KM}]^T. \quad (4)$$

The conditional expectation of $Y = [Y_{11}, \dots, Y_{1M}, Y_{21}, \dots, Y_{2M}, \dots, Y_{KM}]^T$ is then given by

$$E[Y|x, s, d] = \text{diag}(s \otimes d)\Phi(x), \quad (5)$$

where $s \otimes d$ is the Kronecker product of s and d , $\text{diag}(w)$ is a diagonal matrix whose (i, i) th element is equal to the i th element of the vector w , and $\Phi(x)$ is the corresponding raster order of the values $\phi_k(b_m; x)$ given by

$$\Phi(x) = [\phi_1(b_1; x), \phi_1(b_2; x), \dots, \phi_1(b_M; x), \phi_2(b_1; x), \dots, \phi_K(b_M; x)]^T. \quad (6)$$

To simplify notation, we define the forward model vector $f(x, s, d)$ as

$$f(x, s, d) = \text{diag}(s \otimes d)\Phi(x). \quad (7)$$

We use a shot-noise model for the detector noise.^{2,17} The shot-noise model assumes independent noise measurements that are Gaussian with variance proportional to the signal amplitude. This results in the following expression for the conditional density of Y ,

$$p(y|x, s, d, \alpha) = \frac{1}{(\pi\alpha)^P |\Lambda|^{-1}} \exp\left[-\frac{\|y - f(x, s, d)\|_\Lambda^2}{\alpha}\right], \quad (8)$$

where $P = KM$ is the number of measurements, α is an unknown parameter that scales the noise variance, $\Lambda = \text{diag}([1/|y_{11}|, \dots, 1/|y_{1M}|, 1/|y_{21}|, \dots, 1/|y_{KM}|]^T)$, and $\|w\|_\Lambda^2 = w^H \Lambda w$.

We determine x , s , d , and α from the measurements y . Because this is an ill-posed inverse problem, we employ a Bayesian framework to incorporate a prior model for x , the image.² We then maximize the posterior probability of x jointly with respect to y , s , d , and α . This yields the estimators

$$\begin{aligned} & (\hat{x}_{\text{MAP}}, \hat{s}, \hat{d}, \hat{\alpha}) \\ &= \arg \max_{(x \geq 0, s, d, \alpha)} \{\log p(x|y, s, d, \alpha)\} \\ &= \arg \max_{(x \geq 0, s, d, \alpha)} \{\log p(y|x, s, d, \alpha) + \log p(x)\}, \quad (9) \end{aligned}$$

where $p(y|x, s, d, \alpha)$ is the data likelihood and $p(x)$ is the prior model for the image. The estimate \hat{x}_{MAP} is essentially the maximum *a posteriori* (MAP) estimate of the image, but it is computed by simultaneously optimizing with respect to the unknown parameters s , d , and α . Quantities such as s , d , and α are sometimes known as nuisance parameters, because they are not of direct interest but are required for accurate estimation of the desired quantity x . A variety of methods have been proposed for estimating such parameters. These methods range from true maximum-likelihood estimation with Monte Carlo Markov chain techniques,^{18–20} to joint MAP estimation of the unknown image and parameters.^{21,22} Our method is a form of joint MAP estimation, but with a uniform (i.e., improper) prior distribution for s , d , and α . It is worth noting that such estimators can behave poorly in certain cases.²³ However, when the number of measurements is large compared with the dimensionality of the unknowns, as in our case for s , d , and α , these estimators generally work well.

We use the generalized Gaussian Markov random field prior model²⁴ for the image x ,

$$\begin{aligned} p(x) &= p([\mu_a(r_1), \mu_a(r_2), \dots, \mu_a(r_N)]^T) \\ &\quad \times p([D(r_1), D(r_2), \dots, D(r_N)]^T) \\ &= \left[\frac{1}{\sigma_0^N z(p_0)} \exp\left(-\frac{1}{p_0 \sigma_0^{p_0}} \sum_{\{i,j\} \in \mathcal{N}} b_{0,i-j} |x_i - x_j|^{p_0}\right) \right] \\ &\quad \times \left[\frac{1}{\sigma_1^N z(p_1)} \exp\left(-\frac{1}{p_1 \sigma_1^{p_1}} \sum_{\{i,j\} \in \mathcal{N}} b_{1,i-j} |x_{N+i} - x_{N+j}|^{p_1}\right) \right] \\ &= \prod_{u=0}^1 \left[\frac{1}{\sigma_u^N z(p_u)} \exp\left(-\frac{1}{p_u \sigma_u^{p_u}} \right. \right. \\ &\quad \left. \left. \times \sum_{\{i,j\} \in \mathcal{N}} b_{u,i-j} |x_{uN+i} - x_{uN+j}|^{p_u}\right) \right], \quad (10) \end{aligned}$$

where σ_0 and σ_1 are normalization parameters for μ_a and D , respectively, and $1 \leq p_0 \leq 2$ and $1 \leq p_1 \leq 2$ control the degree of edge smoothness for μ_a and D , respectively. The set \mathcal{N} consists of all pairs of adjacent grid points, $z(p_0)$ and $z(p_1)$ are normalization constants, and $b_{0,i-j}$ and $b_{1,i-j}$ represent the coefficients assigned to neighbors i and j for μ_a and D , respectively. This prior model en-

forces smoothness in the solution while preserving sharp edge transitions, and its effectiveness for this kind of problem has been shown previously.²

3. OPTIMIZATION

Let $c(x, s, d, \alpha)$ denote the cost function to be minimized in Eq. (9). Then using the models of Eqs. (8) and (10) and removing constant terms results in

$$\begin{aligned} c(x, s, d, \alpha) &= \frac{1}{\alpha} \|y - f(x, s, d)\|_{\Lambda}^2 + P \log \alpha \\ &\quad + \sum_{u=0}^1 \frac{1}{p_u \sigma_u^{p_u}} \sum_{\{i,j\} \in \mathcal{N}} b_{u,i-j} |x_{uN+i} - x_{uN+j}|^{p_u}. \quad (11) \end{aligned}$$

The objective is then to compute

$$(\hat{x}_{\text{MAP}}, \hat{s}, \hat{d}, \hat{\alpha}) = \arg \min_{(x \geq 0, s, d, \alpha)} c(x, s, d, \alpha). \quad (12)$$

To solve this problem, we adapt the iterative coordinate decent (ICD) method.² The ICD method works by sequentially updating parameters of the optimization, so that each update monotonically reduces the cost function. Previous implementations of ICD sequentially updated pixels in the vector x . Here we generalize the ICD method so that the parameters s , d , and α are also included in the sequence of updates. More specifically, in each iteration of the ICD algorithm, s , d , α , and x are updated sequentially through the relations

$$\hat{\alpha} \leftarrow \arg \min_{\alpha} c(\hat{x}, \hat{s}, \hat{d}, \alpha), \quad (13)$$

$$\hat{s} \leftarrow \arg \min_s c(\hat{x}, s, \hat{d}, \hat{\alpha}), \quad (14)$$

$$\hat{d} \leftarrow \arg \min_d c(\hat{x}, \hat{s}, d, \hat{\alpha}), \quad (15)$$

$$\hat{x} \leftarrow \text{ICD_update}_x\{c(x, \hat{s}, \hat{d}, \hat{\alpha}), \hat{x}\}, \quad (16)$$

where the ICD_update_x operation performs one iteration of ICD optimization to reduce the cost function $c(\cdot, \hat{s}, \hat{d}, \hat{\alpha})$ starting at the initial value \hat{x} . The result of ICD_update_x is then used to update the value of \hat{x} . Iterative application of these update equations produces a convergent sequence of decreasing costs.

The updates of Eqs. (13), (14), and (15) can be calculated in closed form by setting the partial derivative with respect to each variable to zero and solving the resulting equations to yield

$$\hat{\alpha} \leftarrow \frac{1}{P} \|y - f(\hat{x}, \hat{s}, \hat{d})\|_{\Lambda}^2, \quad (17)$$

$$\hat{s}_k \leftarrow \frac{[\text{diag}(\hat{d})\Phi_k^{(s)}(\hat{x})]^H \Lambda_k^{(s)} y}{\|\text{diag}(\hat{d})\Phi_k^{(s)}(\hat{x})\|_{\Lambda_k^{(s)}}^2}, \quad k = 1, 2, \dots, K, \quad (18)$$

$$\hat{d}_m \leftarrow \frac{[\text{diag}(\hat{s})\Phi_m^{(d)}(\hat{x})]^H \Lambda_m^{(d)} y}{\|\text{diag}(\hat{s})\Phi_m^{(d)}(\hat{x})\|_{\Lambda_m^{(d)}}^2}, \quad m = 1, 2, \dots, M, \quad (19)$$

where H denotes the Hermitian transpose, $\Lambda_k^{(s)} = \text{diag}([1/|y_{k1}|, 1/|y_{k2}|, \dots, 1/|y_{kM}|]^T)$ and $\Lambda_m^{(d)} = \text{diag}([1/|y_{1m}|, 1/|y_{2m}|, \dots, 1/|y_{K_m}|]^T)$ are the inverse diagonal covariance matrices associated with source k and detector m , respectively, and $\Phi_k^{(s)}(\hat{x}) = [\phi_k(b_1; \hat{x}), \phi_k(b_2; \hat{x}), \dots, \phi_k(b_M; \hat{x})]^T$ and $\Phi_m^{(d)}(\hat{x}) = [\phi_1(b_m; \hat{x}), \phi_2(b_m; \hat{x}), \dots, \phi_{K_m}(b_m; \hat{x})]^T$ are the complex amplitude vectors associated with source k and detector m , respectively.

The update of the variable x in Eq. (16) is of course more difficult since x is a high-dimensional vector, particularly in the 3-D case. To update the image, we use one scan of the ICD algorithm as an ICD_update_x operation. One ICD scan involves sequentially updating each element of x with random ordering, and incorporation of the updated elements as the scan progresses. During this scan each element of x is updated only once. At the

$$\hat{x}_{uN+i} \leftarrow \arg \min_{x_{uN+i} \geq 0} \left\{ \frac{1}{\hat{\alpha}} \|y - f(\hat{x}, \hat{s}, \hat{d})\|_{\Lambda}^2 - [f'(\hat{x}, \hat{s}, \hat{d})]_{*(uN+i)}(x_{uN+i} - \hat{x}_{uN+i})\|_{\Lambda}^2 + \frac{1}{P_u \sigma_u^{P_u}} \sum_{j \in \mathcal{N}_i} b_{u,i-j} |x_{uN+i} - \hat{x}_{uN+j}|^{P_u} \right\}, \quad (23)$$

where $[f'(\hat{x}, \hat{s}, \hat{d})]_{*(uN+i)}$ is the $(uN + i)$ th column of the Fréchet derivative matrix and \mathcal{N}_i is the set of grid points neighboring grid point i . To compute the solution to Eq. (23), we express the first term as a quadratic function of x_{uN+i} and then perform a one-dimensional minimization that is solved by a half-interval search for the root of the analytical derivative.²

The Fréchet derivative $f'(\hat{x}, \hat{s}, \hat{d})$ is a $P \times 2N$ complex matrix given by

$$f'(\hat{x}, \hat{s}, \hat{d}) = \begin{bmatrix} \frac{\partial f_{11}(\hat{x}, \hat{s}_1, \hat{d}_1)}{\partial \mu_a(r_1)} & \dots & \frac{\partial f_{11}(\hat{x}, \hat{s}_1, \hat{d}_1)}{\partial \mu_a(r_N)} & \frac{\partial f_{11}(\hat{x}, \hat{s}_1, \hat{d}_1)}{\partial D(r_1)} & \dots & \frac{\partial f_{11}(\hat{x}, \hat{s}_1, \hat{d}_1)}{\partial D(r_N)} \\ \frac{\partial f_{12}(\hat{x}, \hat{s}_1, \hat{d}_2)}{\partial \mu_a(r_1)} & \dots & \frac{\partial f_{12}(\hat{x}, \hat{s}_1, \hat{d}_2)}{\partial \mu_a(r_N)} & \frac{\partial f_{12}(\hat{x}, \hat{s}_1, \hat{d}_2)}{\partial D(r_1)} & \dots & \frac{\partial f_{12}(\hat{x}, \hat{s}_1, \hat{d}_2)}{\partial D(r_N)} \\ \vdots & \ddots & \vdots & \vdots & \ddots & \vdots \\ \frac{\partial f_{1M}(\hat{x}, \hat{s}_1, \hat{d}_M)}{\partial \mu_a(r_1)} & \dots & \frac{\partial f_{1M}(\hat{x}, \hat{s}_1, \hat{d}_M)}{\partial \mu_a(r_N)} & \frac{\partial f_{1M}(\hat{x}, \hat{s}_1, \hat{d}_M)}{\partial D(r_1)} & \dots & \frac{\partial f_{1M}(\hat{x}, \hat{s}_1, \hat{d}_M)}{\partial D(r_N)} \\ \frac{\partial f_{21}(\hat{x}, \hat{s}_2, \hat{d}_1)}{\partial \mu_a(r_1)} & \dots & \frac{\partial f_{21}(\hat{x}, \hat{s}_2, \hat{d}_1)}{\partial \mu_a(r_N)} & \frac{\partial f_{21}(\hat{x}, \hat{s}_2, \hat{d}_1)}{\partial D(r_1)} & \dots & \frac{\partial f_{21}(\hat{x}, \hat{s}_2, \hat{d}_1)}{\partial D(r_N)} \\ \vdots & \ddots & \vdots & \vdots & \ddots & \vdots \\ \frac{\partial f_{KM}(\hat{x}, \hat{s}_K, \hat{d}_M)}{\partial \mu_a(r_1)} & \dots & \frac{\partial f_{KM}(\hat{x}, \hat{s}_K, \hat{d}_M)}{\partial \mu_a(r_N)} & \frac{\partial f_{KM}(\hat{x}, \hat{s}_K, \hat{d}_M)}{\partial D(r_1)} & \dots & \frac{\partial f_{KM}(\hat{x}, \hat{s}_K, \hat{d}_M)}{\partial D(r_N)} \end{bmatrix}, \quad (24)$$

beginning of an ICD scan, the nonlinear functional $f(x, s, d)$ is first expressed by use of a Taylor expansion as

$$\|y - f(x, \hat{s}, \hat{d})\|_{\Lambda}^2 \approx \|y - f(\hat{x}, \hat{s}, \hat{d}) - f'(\hat{x}, \hat{s}, \hat{d})\Delta x\|_{\Lambda}^2, \quad (20)$$

where $\Delta x = x - \hat{x}$ and $f'(\hat{x}, \hat{s}, \hat{d})$ represents the Fréchet derivative of $f(x, \hat{s}, \hat{d})$ with respect to x at $x = \hat{x}$. With relation (20), an approximate cost function for the original problem is

$$c(x, \hat{s}, \hat{d}, \hat{\alpha}) \approx \frac{1}{\hat{\alpha}} \|z - f'(\hat{x}, \hat{s}, \hat{d})x\|_{\Lambda}^2 + \sum_{u=0}^1 \frac{1}{P_u \sigma_u^{P_u}} \sum_{\{i,j\} \in \mathcal{N}} b_{u,i-j} |x_{uN+i} - x_{uN+j}|^{P_u}, \quad (21)$$

where

$$z = y - f(\hat{x}, \hat{s}, \hat{d}) + f'(\hat{x}, \hat{s}, \hat{d})\hat{x}. \quad (22)$$

Then, with the other image elements fixed, the ICD update for \hat{x}_{uN+i} is given by

where the first N columns correspond to the μ_a components of x and the remaining N columns correspond to the D components. In a similar manner to the Fréchet derivative commonly used for unity coupling coefficients,²⁵ it can be shown that each element of the matrix is given by

$$\frac{\partial f_{km}(\hat{x}, \hat{s}_k, \hat{d}_m)}{\partial \mu_a(r_i)} = -\hat{s}_k \hat{d}_m g(b_m, r_i; \hat{x}) \phi_k(r_i; \hat{x}) A, \quad (25)$$

$$\frac{\partial f_{km}(\hat{x}, \hat{s}_k, \hat{d}_m)}{\partial D(r_i)} = -\hat{s}_k \hat{d}_m \nabla g(b_m, r_i; \hat{x}) \cdot \nabla \phi_k(r_i; \hat{x}) A, \quad (26)$$

where A is the voxel volume, the Green's function $g(b_m, r_i; \hat{x})$ is the solution of Eq. (1) for a point source located at b_m [i.e., by setting $a_k \leftarrow b_m$ in Eq. (1), with use of reciprocity to reduce computation¹⁷] and a given image \hat{x} , ∇ is the spatial gradient operator with respect to r_i , and domain discretization errors are ignored. Note that the Fréchet derivative is proportional to the product $\hat{s}_k \hat{d}_m$, so that if the coupling coefficients are not accurately estimated, formulas (25) and (26) do not yield accurate Fréchet derivatives, and thus the computed gradient

```

main {
  1. Initialize  $\hat{x}$  with a background absorption and diffusion coefficient estimate.
  2. Repeat until converged: {
    (a)  $\hat{\alpha} \leftarrow \frac{1}{P} \|y - f(\hat{x}, \hat{s}, \hat{d})\|_{\Lambda}^2$  Eq.(17)
    (b)  $\hat{s}_k \leftarrow \frac{[\text{diag}(\hat{d}) \Phi_k^{(s)}(\hat{x})]^H \Lambda_k^{(s)} y}{\|\text{diag}(\hat{d}) \Phi_k^{(s)}(\hat{x})\|_{\Lambda_k^{(s)}}^2}$  Eq.(18)
         $k = 1, 2, \dots, K$ 
    (c)  $\hat{d}_m \leftarrow \frac{[\text{diag}(\hat{s}) \Phi_m^{(d)}(\hat{x})]^H \Lambda_m^{(d)} y}{\|\text{diag}(\hat{s}) \Phi_m^{(d)}(\hat{x})\|_{\Lambda_m^{(d)}}^2}$  Eq.(19)
         $m = 1, 2, \dots, M$ 
    (d)  $\hat{x} \leftarrow \text{ICD\_update}_x \{c(x, \hat{s}, \hat{d}, \hat{\alpha}), \hat{x}\}$  Eq.(16)
  }
}

```

(a)

```

ICD_update_x {c(x,  $\hat{s}$ ,  $\hat{d}$ ,  $\hat{\alpha}$ ),  $\hat{x}$ } {
  1. Compute  $\phi_k(\cdot; \hat{x})$ ,  $k = 1, 2, \dots, K$  and  $g(b_m, \cdot; \hat{x})$ ,  $m = 1, 2, \dots, M$ .
  2. For  $u = 0, 1$ ,
    For  $i = 1, \dots, N$  (in random order), {
      (a) Compute  $[f'(\hat{x}, \hat{s}, \hat{d})]_{*(uN+i)}$  with (24)-(26).
      (b) Update  $x_{uN+i}$ , as described by Ye, et al.2
      
$$\hat{x}_{uN+i} \leftarrow \arg \min_{x_{uN+i} \geq 0} \left\{ \frac{1}{\hat{\alpha}} \left\| y - f(\hat{x}, \hat{s}, \hat{d}) - [f'(\hat{x}, \hat{s}, \hat{d})]_{*(uN+i)} (x_{uN+i} - \hat{x}_{uN+i}) \right\|_{\Lambda}^2 \right.$$

      
$$\left. + \frac{1}{p_u \sigma^{p_u}} \sum_{j \in \mathcal{N}_i} b_{u,i-j} |x_{uN+i} - \hat{x}_{uN+j}|^{p_u} \right\}$$
 Eq.(23)
    }
  3. Return  $\hat{x}$ .
}

```

(b)

Fig. 1. Pseudocode specification for (a) the overall optimization procedure and (b) the image update by one ICD scan.

direction of the cost function in Eq. (12) is not accurate. Therefore, estimation of the coupling coefficients is essential for accurate image reconstruction.

The dimensions of the Fréchet derivative matrix are very large for practical 3-D imaging. For example, $(KM \times 2N \times 8) = 790$ Mbytes of memory are needed to store the Fréchet derivative matrix for 30 sources, 48 detectors, and a $33 \times 33 \times 33$ grid point image if 4 bytes are used for a real number. However, the storage can be reduced by exploiting two facts. First, only the $(uN + i)$ th column of the Fréchet derivative matrix is needed to update x_{uN+i} , as seen in Eq. (23). Second, the Fréchet derivative in Eqs. (25) and (26) is separable into the $\phi_k(r_i; \hat{x})$ term and the $g(b_m, r_i; \hat{x})$ term. Thus we compute only $\phi_k(\cdot; \hat{x})$ for $k = 1, 2, \dots, K$ and $g(b_m, \cdot; \hat{x})$ for $m = 1, 2, \dots, M$ before the ICD update of the whole image; and then when x_i is updated, the i th column of the Fréchet derivative is computed with these vectors. This method, which involves storing the forward solutions for all sources, the Green's function for all detectors, and only one column of the Fréchet derivative matrix, reduces the required memory to $(KN + MN + KM) \times 8$ bytes without requiring additional computation. In the above example, the required memory is then only 22 Mbytes.

Note that this implementation differs from the work of Ye *et al.*,^{2,3} where they did not need to consider this storage issue because they dealt with a two-dimensional problem. The whole optimization procedure is summarized in the pseudocode of Fig. 1.

4. RESULTS

A. Simulation

The performance of the algorithm described above was investigated by simulation with cubic tissue phantoms of dimension $8 \times 8 \times 8$ cm on an edge and with background $D = 0.03$ cm and $\mu_a = 0.02$ cm⁻¹. Two phantoms were used. Phantom A has two spherical μ_a inhomogeneities with diameters of 2.25 cm and 2.75 cm and central values of 0.070 cm⁻¹ that decay smoothly as a fourth-order polynomial to the background value, and two spherical D inhomogeneities with diameters of 2.25 cm and a central value of 0.01 cm that increase smoothly to the background value as a fourth-order polynomial. Phantom A is shown as an isosurface plot in Figs. 2(a) and 2(b) and as gray-scale plots of cross sections in Figs. 3(a) and 3(b). Phantom B has a high absorption inhomogeneity with a peak

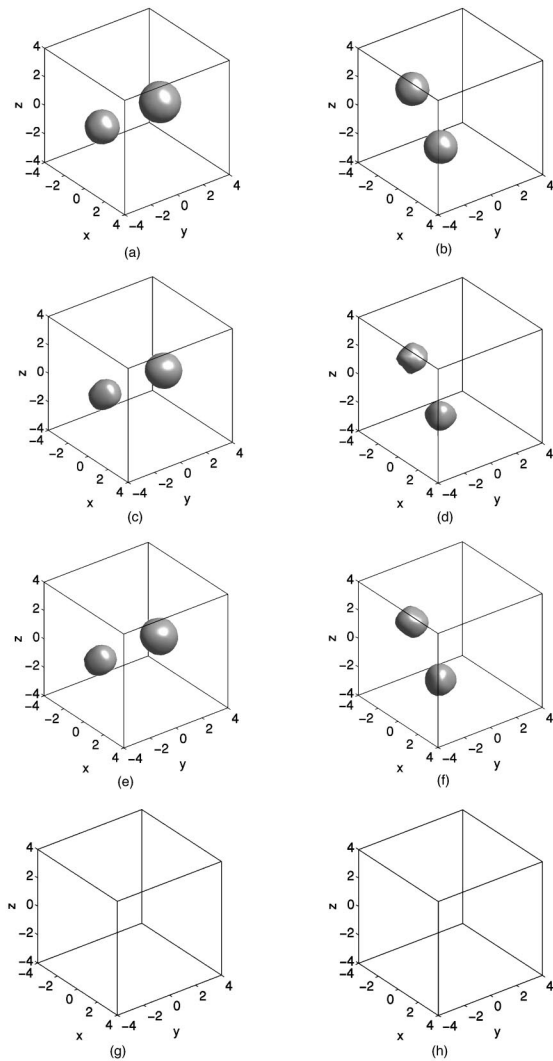


Fig. 2. Isosurface plots at 0.04 cm^{-1} and 0.02 cm , respectively, for μ_a (left column) and D (right column) for Phantom A: (a), (b) original tissue phantom; (c), (d) reconstructions with source-detector calibration; (e), (f) reconstructions using the correct weights; (g), (h) reconstructions without calibration.

value of $\mu_a = 0.07 \text{ cm}^{-1}$ near one face of the cube and a low diffusion inhomogeneity near the center with a diameter of 2.75 cm and a central value of 0.01 cm that increases smoothly as a fourth-order polynomial to the background value, as shown in Figs. 4(a) and 4(b) and Figs. 5(a) and 5(b). Phantom B was used to assess whether an absorber close to a set of sources and detectors is difficult to reconstruct, since its effect might be compensated for by reduced source and detector coupling coefficients.

Five sources, with a modulation frequency of 100 MHz , and eight detectors are located on each face [Fig. 6(a)], yielding $K = 30$ and $M = 48$. Shot noise was added to the data, and the average signal-to-noise ratio for sources and detectors on opposite faces was 33 dB . The complex source-detector coupling coefficients (a total of 78 parameters) were generated with a Gaussian distribution centered at $1 + j0$ and having a standard deviation of $(\sigma_{\text{coeff}}/\sqrt{2})(1 + j)$, with $\sigma_{\text{coeff}} = 0.5$ [Fig. 7(a)]. The domain was discretized onto $33 \times 33 \times 33$ grid points, and

the forward model [Eq. (1)] was solved by using finite differences. Referring to Fig. 6(b), a zero-flux ($\phi = 0$) boundary condition on the outer boundary provides the approximate boundary condition on the physical boundary.^{2,17} The sources and detectors were placed 0.6 times the grid point spacing in from the zero-flux boundary, achieved through appropriate weighting of the nearest grid points. Only nodes within the imaging boundary were updated, which excludes the three outermost layers of grid points, to avoid singularities near the sources and detectors. The optimization was initialized by using the homogeneous values $D = 0.03 \text{ cm}$ and $\mu_a = 0.02 \text{ cm}^{-1}$. The image prior model used $p_0 = 2.0$, $\sigma_0 = 0.01 \text{ cm}^{-1}$, $p_1 = 2.0$, and $\sigma_1 = 0.004 \text{ cm}$.

Reconstructions of μ_a and D after 30 iterations are shown in Figs. 2(c) and 2(d) and Figs. 3(c) and 3(d) for Phantom A, and in Figs. 4(c) and 4(d) and Figs. 5(c) and 5(d) for Phantom B. The corresponding images reconstructed with the correct values of coupling coefficients are shown for comparison in Figs. 2(e) and 2(f), Figs. 3(e) and 3(f), Figs. 4(e) and 4(f), and Figs. 5(e) and 5(f). Our algorithm reconstructs images quite similar to those reconstructed when the true values of the coupling coefficients are used. The corresponding images reconstructed

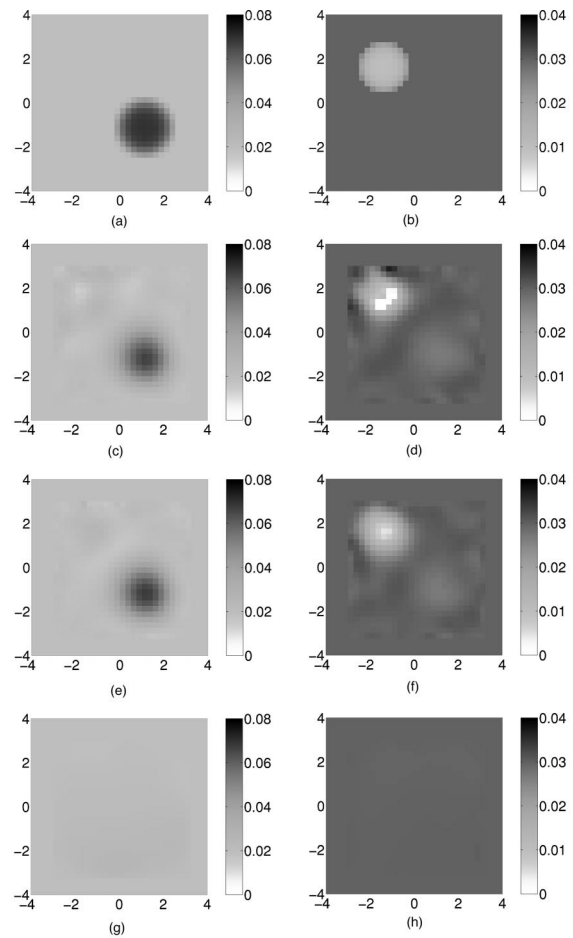


Fig. 3. Cross sections through the centers of the inhomogeneities at $z = 0.5 \text{ cm}$ and $z = 1.5 \text{ cm}$, respectively, for μ_a (left column) and D (right column) of Phantom A: (a), (b) original tissue phantom; (c), (d) reconstructions with source-detector calibration; (e), (f) reconstructions using the correct weights; (g), (h) reconstructions without calibration.

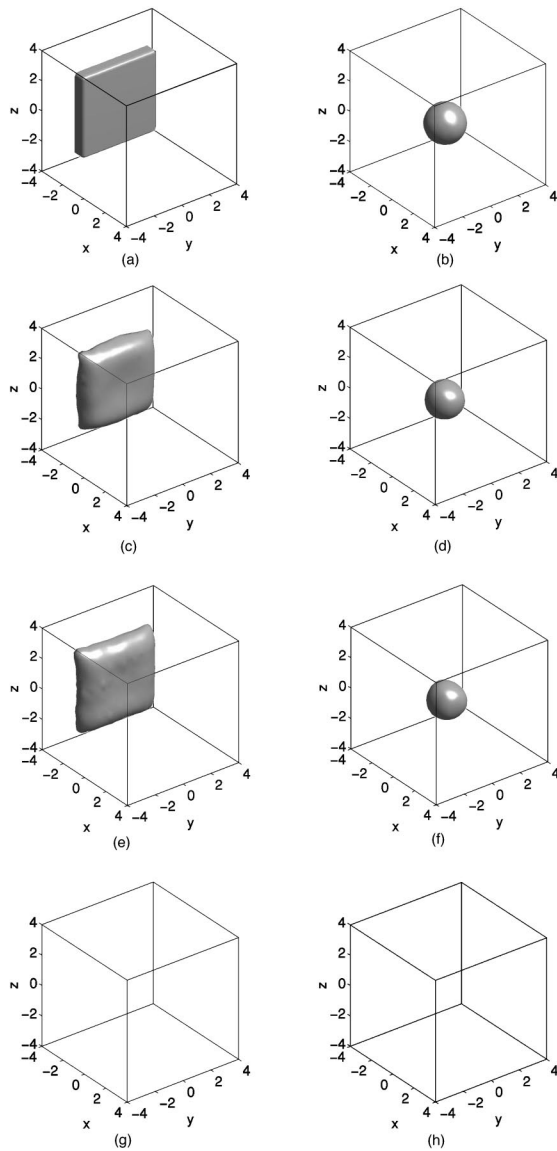


Fig. 4. Isosurface plots at 0.04 cm^{-1} and 0.02 cm , respectively, for μ_a (left column) and D (right column) for Phantom B: (a), (b) original tissue phantom; (c), (d) reconstructions with source-detector calibration; (e), (f) reconstructions using the correct weights; (g), (h) reconstructions without calibration.

with all coupling coefficients set to $1 + j0$ are shown in Figs. 2(g) and 2(h), Figs. 3(g) and 3(h), Figs. 4(g) and 4(h), and Figs. 5(g) and 5(h). These show that poor reconstructions are obtained if the source-detector coupling is not accounted for in the reconstruction process. This is due to the effectively incorrect forward model and hence incorrect Fréchet derivatives. In fact, for the large range of source and detector coupling coefficients used in these examples, the images reconstructed without calibration differ little from the initial starting point of the optimization, when the coupling coefficients are fixed at $1 + j0$. The convergence of the normalized root mean square error (NRMSE) between the phantoms and the reconstructed images is shown in Fig. 8. The NRMSE is defined by

$$\text{NRMSE} = \left[\frac{1}{2} \sum_{u=0}^1 \frac{\sum_{r_i \in R} |\hat{x}_{uN+i} - x_{uN+i}|^2}{\sum_{r_i \in R} |x_{uN+i}|^2} \right]^{1/2}, \quad (27)$$

where R is the set of the updated grid points within the imaging boundary [shown in Fig. 6(b)], \hat{x}_{uN+i} is the reconstructed value of the $(uN + i)$ th image element, and x_{uN+i} is the correct value. The NRMSE obtained with the reconstruction incorporating calibration is similar to that obtained when the correct coupling coefficients are used. However, if calibration is not used, there is little decrease in the NRMSE from the starting value.

The accuracy of the estimated coupling coefficients is shown in Figs. 7(b) and 7(c), where the differences between the true coupling coefficients and those estimated after 30 iterations is given. The root-mean-square (RMS) error of the coupling coefficients after 30 iterations is 0.011 for Phantom A and 0.017 for Phantom B, which are only 2% and 3% of the standard deviation of the coupling coefficients, respectively, indicating accurate recovery. Figure 9(a) shows the variation of the RMS error between the estimated and the true coupling coefficients versus it-

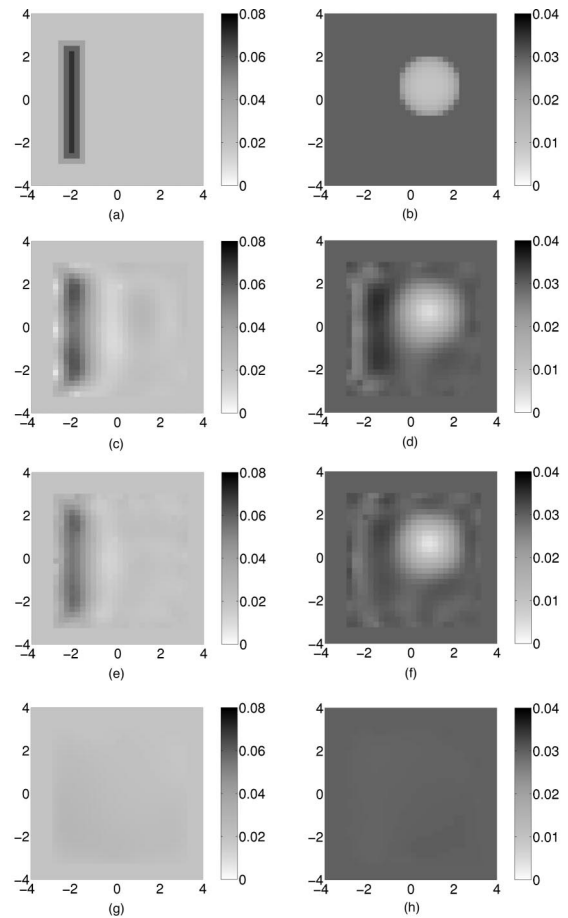


Fig. 5. Cross sections through the centers of the inhomogeneities at $z = 0.0 \text{ cm}$ and $z = 0.25 \text{ cm}$, respectively, for μ_a (left column) and D (right column) of Phantom B: (a), (b) original tissue phantom; (c), (d) reconstructions with source-detector calibration; (e), (f) reconstructions using the correct weights; (g), (h) reconstructions without calibration.

eration, showing good convergence in only a few iterations. The results therefore indicate that our algorithm reconstructs accurate images without prior calibration by the estimation of the coupling coefficients in an efficient optimization scheme.

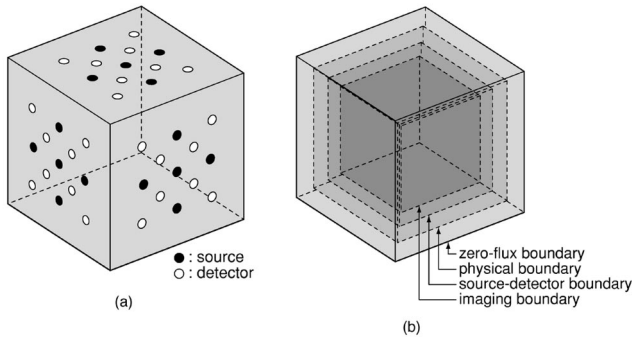


Fig. 6. (a) Locations of sources and detectors, (b) several levels of boundaries: from outer boundary, zero-flux boundary, physical boundary, source-detector boundary, and imaging boundary.

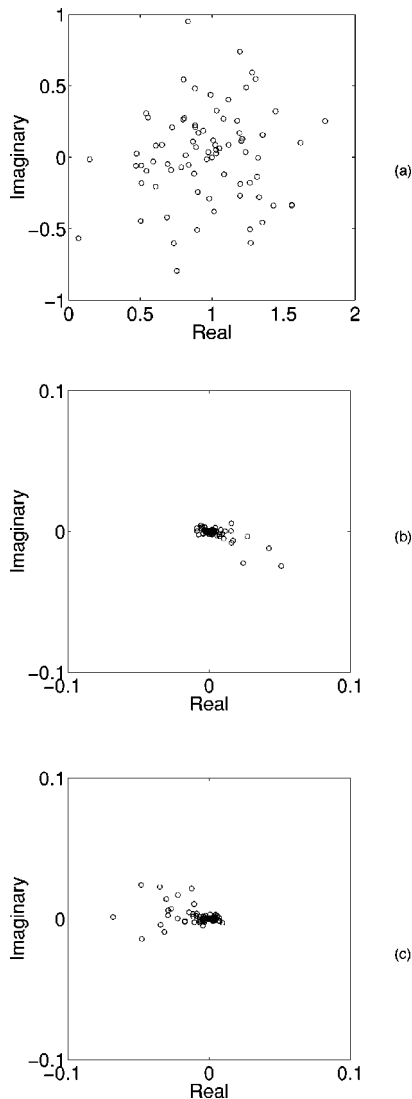


Fig. 7. (a) Source-detector coupling coefficients used in the simulations. Estimation error of coupling coefficients for (b) Phantom A and (c) Phantom B after 30 iterations. Note that the scale of (b) and (c) is 10 times of that of (a).

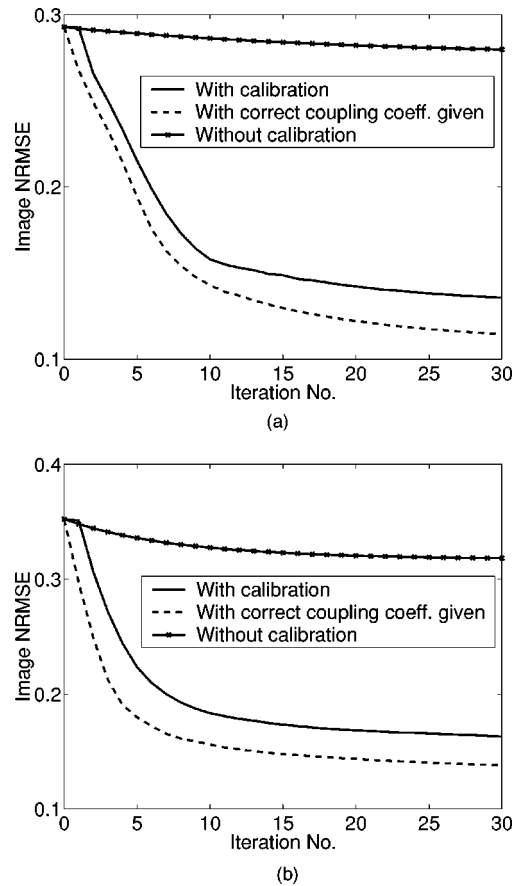


Fig. 8. NRMSE between the phantom and the reconstructed images for (a) Phantom A and (b) Phantom B.

For Phantom B, the absorber close to one source-detector plane is reconstructed quite accurately and is not distorted by the variable coupling coefficients of the sources and detectors. Some small spikes of low μ_a appear in the neighborhood of some of the sources and detectors [Fig. 5(c)], but the effect is quite small. However, the final NRMSE is somewhat larger for Phantom B than for Phantom A (Fig. 8), and the real part of some of the coupling coefficients is underestimated [Fig. 7(c)]. We categorize the sources and detectors on the side nearest the absorber as Group 1, and the remainder as Group 2. Most of the underestimated coefficients are those for sources and detectors on the face close to the absorber. The estimation error for these coupling coefficients (Group 1) is larger than the remaining sources and detectors [Fig. 9(b)]. Therefore, because the light transmitted through the absorber is highly attenuated, it is partially compensated for by reduced estimated coupling coefficients. As noted above, however, the effect is quite small.

To study the effect of the variability of the coupling coefficients, reconstructions were performed (30 iterations) for Phantom A for different standard deviations of (real and imaginary parts of) the coupling coefficients σ_{coeff} . The coupling coefficients were generated with a Gaussian distribution centered at $1 + j0$ and having $(\sigma_{\text{coeff}}/\sqrt{2})(1 + j)$. The image NRMSE is compared for various standard derivations in Fig. 10. Estimating the calibration coefficients reduces the NRMSE, as expected. The error without calibration did not increase beyond ~ 0.28 with

increasing σ_{coeff} , as this value for the image NRMSE corresponds to the initial value with the correct background parameters and indicates that a useful image is not recovered. Figures 10 and 11 show that the quality of the uncalibrated reconstruction degrades rapidly as σ_{coeff} is increased for values of $\sigma_{\text{coeff}} < 0.1$. This result indicates that accurate estimation of the coupling coefficients is crucial for determining accurate images. The value of σ_{coeff} will obviously be a function of the specific experimental arrangement. Figure 10 illustrates the effect of variations in the source–detector coupling. While some experimental arrangements may have (approximately) a single, scalar source–detector weight,¹⁴ it is still important to determine this value.

We have previously established that multiresolution techniques such as multigrid achieve more reliable convergence of the cost function while dramatically reducing the computation time in two-dimensional optical diffusion tomography.³ The approach presented for extracting the source–detector weights as part of the image reconstruction in a Bayesian framework could be extended to multiresolution approaches. We investigated a simple multiresolution approach by using a coarse-grid solution ($17 \times 17 \times 17$) to initialize a fine-grid solution ($33 \times 33 \times 33$). Better convergence was achieved by using this simple two-grid approach with various initial conditions consisting of uniform D and μ_a differing from the true background by as much as a factor of 3. This performance improvement occurs both with known and estimated source–detector weights. Also, we noticed that in some cases with a fixed, fine grid, the cost function with variable source–detector weights was slightly larger than that with the true weights. Although the images in these cases were still excellent, the additional degrees of freedom should have resulted in a smaller value of the cost function. With the multiresolution approach this was indeed the case, providing further evidence of the robustness of our approach. We emphasize that the algorithm that we present for extraction of the source–detector weights in a Bayesian framework was consistently effective, regardless of the particular iterative reconstruction approach.

B. Experiment

The effectiveness of our source–detector calibration approach was evaluated for measurements made on an optically clear culture flask containing a black plastic cylinder embedded in a turbid Intralipid suspension [Fig. 12(a)]. The plastic cylinder was embedded in a 0.5% concentration of Intralipid. The data were collected with an inexpensive apparatus comprised of an infrared LED operating at 890 nm and a silicon p-i-n photodiode, as schematically depicted in Fig. 12(b). With the source centrally located, as shown in Fig. 12(b), the detector located on the other side of the flask was mechanically scanned in the same plane as the source, and data were taken at 25 symmetrical locations (referring to the abscissa of Fig. 13, -2.4 to 2.4 cm in steps of 0.2 cm). The flask was rotated so that the relative positions of source and detector were reversed, and another set of data was taken. This resulted in a total of two source positions with 25 detector measurements each. The sources were modulated at 50

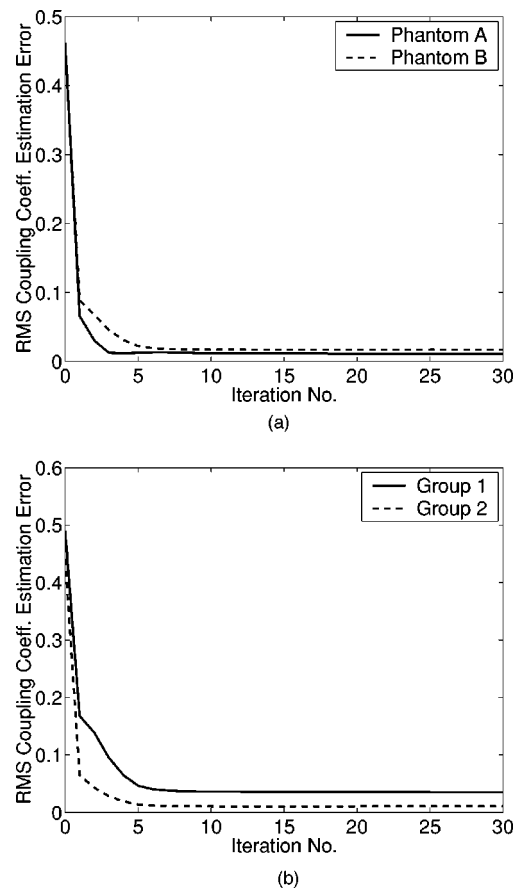


Fig. 9. (a) RMS error in the estimated coupling coefficients versus iteration, (b) convergence of coupling coefficients for Group 1 (—) and Group 2 (---) for Phantom B.

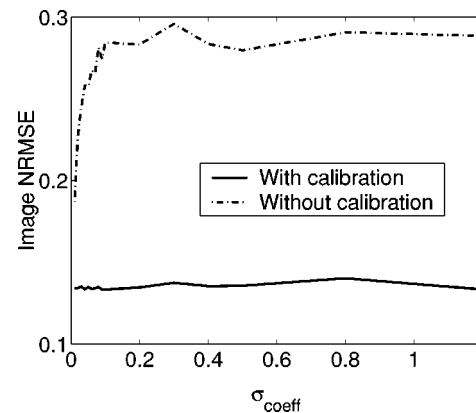


Fig. 10. Image NRMSE comparison between the reconstruction with coupling coefficient calibration and the reconstruction with coupling coefficients fixed to $1 + j0$, for various standard deviations of coupling coefficients. Images were obtained after 30 iterations.

MHz. The measured data were normalized to a free-space calibration measurement. This experimental arrangement is similar to one we used previously,^{14,26} but with two sources instead of one.

Each set of 25 measurements used a single detector that was translated, so only one detector calibration parameter was associated with these measurements. Because the detector was associated with only one source,

the source calibration parameter can be included in the detector calibration parameter. As the position of the flask relative to the source and detector may not be exactly the same after it is rotated, a different detector calibration coefficient was used for the second set of 25 measurements. Therefore, a total of two complex coupling coefficients were used for this experiment.

Inversions were performed for the absorption coefficients and coupling coefficients, assuming D known. The domain was discretized into $65 \times 33 \times 65$ grid points. For computational efficiency, we used a simple multiresolution technique in which 200 coarse-grid ($33 \times 17 \times 33$) iterations were followed by 30 fine-grid iterations. We used $\sigma_0 = 1.0 \text{ cm}^{-1}$ and $p_0 = 2.0$ for the image prior model.

Figure 13 shows reconstructed images of the absorption coefficient in the measurement plane. Figure 13(a) shows the reconstruction obtained with two complex-valued calibration coefficients; Fig. 13(b) shows the reconstruction obtained when only a single complex-calibration coefficient was used (i.e., the two coefficients were assumed equal); Fig. 13(c) shows the reconstruction obtained with a single real-valued calibration coefficient; and, finally, Fig. 13(d) assumed all calibration coefficients to be 1. The reconstruction of Fig. 13(a) used the most accurate model and also produced a reconstruction that appears to be most accurate in shape. The estimated values of the calibration coefficients at the final iteration were $4.49 + j0.43$ and $4.42 + j0.43$, respectively. The difference between them was small, suggesting that rotation of the flask did not significantly alter the calibration parameters. Therefore Fig. 13(b) shows almost the same reconstruction quality as Fig. 13(a), but with slightly more artifacts in the neighborhood of the detector locations. Generally, the elliptical shape of the reconstruction in Fig. 13(c) appears to be the least accurate. Figure 13(d) shows that reconstruction without accurate estimation of the calibration coefficients was not possible.

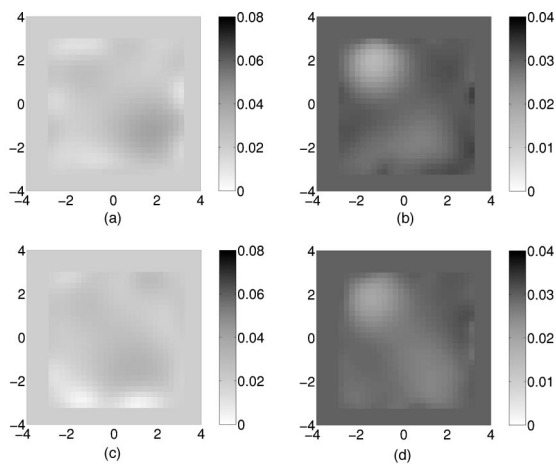
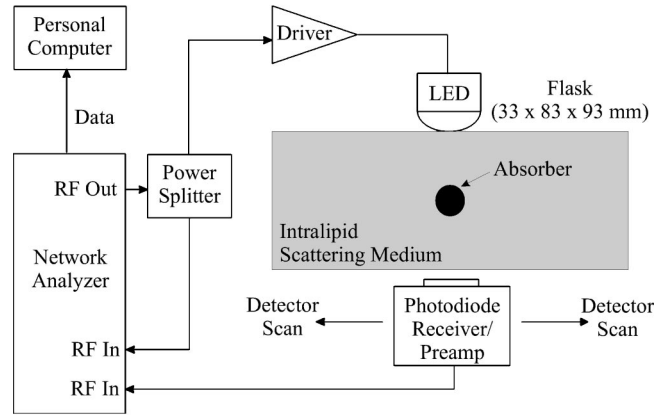


Fig. 11. Cross sections of the reconstructed images of Phantom A without calibration through the centers of the inhomogeneities at $z = 0.5 \text{ cm}$ for μ_a and $z = 1.5 \text{ cm}$ for D for $\sigma_{\text{coeff}} = 0.02$ for (a) μ_a and (b) D and for $\sigma_{\text{coeff}} = 0.04$ for (c) μ_a and (d) D .



(a)



(b)

Fig. 12. (a) Culture flask with the absorbing cylinder embedded in a scattering Intralipid solution, (b) schematic diagram of the apparatus used to collect data.

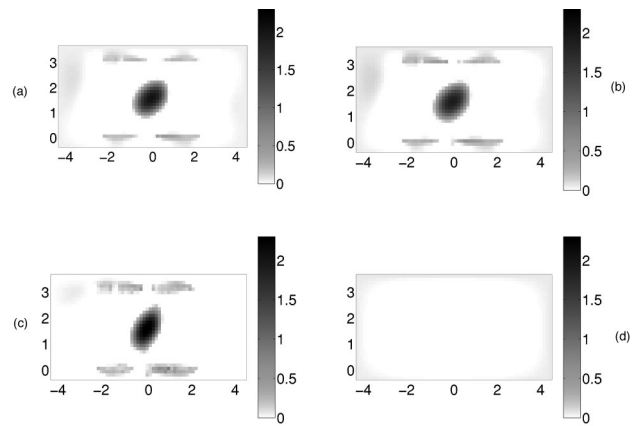


Fig. 13. Cross sections for reconstructed images of an absorbing cylinder with (a) two complex-valued calibration coefficients, (b) a single complex calibration coefficient, (c) a single real calibration coefficient, and (d) all calibration coefficients assumed to be 1.

5. CONCLUSIONS

We have formulated the Bayesian optical diffusion tomography with the source–detector parameter-estimation problem and proposed an efficient optimization scheme. Our algorithm does not require any prior calibration, and it estimates coupling coefficients successfully with only a small amount of additional computation. Simulation and experimental results show that images can be reconstructed along with the accurate estimation of the coupling coefficients.

ACKNOWLEDGMENTS

This work was supported by the National Science Foundation under contract CCR-0073357.

Corresponding author Kevin J. Webb can be reached by e-mail at webb@ecn.purdue.edu.

REFERENCES

1. S. R. Arridge, "Optical tomography in medical imaging," *Inverse Probl.* **15**, R41–R93 (1999).
2. J. C. Ye, K. J. Webb, C. A. Bouman, and R. P. Millane, "Optical diffusion tomography using iterative coordinate descent optimization in a Bayesian framework," *J. Opt. Soc. Am. A* **16**, 2400–2412 (1999).
3. J. C. Ye, C. A. Bouman, K. J. Webb, and R. P. Millane, "Non-linear multigrid algorithms for Bayesian optical diffusion tomography," *IEEE Trans. Image Process.* **10**, 909–922 (2001).
4. S. S. Saquib, K. M. Hanson, and G. S. Cunningham, "Model-based image reconstruction from time-resolved diffusion data," in *Medical Imaging 1997: Image Processing*, K. M. Hanson, ed., *Proc. SPIE* **3034**, 369–380 (1997).
5. S. R. Arridge and M. Schweiger, "A gradient-based optimization scheme for optical tomography," *Opt. Express* **2**, 213–226 (1998), www.opticsexpress.org.
6. A. H. Hielscher, A. D. Klose, and K. M. Hanson, "Gradient-based iterative image reconstruction scheme for time-resolved optical tomography," *IEEE Trans. Med. Imaging* **18**, 262–271 (1999).
7. D. Boas, T. Gaudette, and S. Arridge, "Simultaneous imaging and optode calibration with diffuse optical tomography," *Opt. Express* **8**, 263–270 (2001), www.opticsexpress.org.
8. H. Jiang, K. Paulsen, and U. Osterberg, "Optical image reconstruction using dc data: simulations and experiments," *Phys. Med. Biol.* **41**, 1483–1498 (1996).
9. H. Jiang, K. Paulsen, U. Osterberg, and M. Patterson, "Improved continuous light diffusion imaging in single- and multi-target tissue-like phantoms," *Phys. Med. Biol.* **43**, 675–693 (1998).
10. B. W. Pogue, S. P. Poplack, T. O. McBride, W. A. Wells, K. S. Osterman, U. L. Osterberg, and K. D. Paulsen, "Quantitative hemoglobin tomography with diffuse near-infrared spectroscopy: pilot results in the breast," *Radiology* **218**, 261–266 (2001).
11. B. W. Pogue, C. Willscher, T. O. McBride, U. L. Osterberg, and K. D. Paulsen, "Contrast-detail analysis for detection and characterization with near-infrared diffuse tomography," *Med. Phys.* **27**, 2693–2700 (2000).
12. T. O. McBride, B. W. Pogue, S. Poplack, S. Soho, W. A. Wells, S. Jiang, U. Osterberg, and K. D. Paulsen, "Multi-spectral near-infrared tomography: a case study in compensating for water and lipid content in hemoglobin imaging of the breast," *J. Biomed. Opt.* **7**, 72–79 (2002).
13. N. Iftimia and H. Jiang, "Quantitative optical image reconstructions of turbid media by use of direct-current measurements," *Appl. Opt.* **39**, 5256–5261 (2000).
14. A. B. Milstein, S. Oh, J. S. Reynolds, K. J. Webb, C. A. Bouman, and R. P. Millane, "Three-dimensional Bayesian optical diffusion tomography using experimental data," *Opt. Lett.* **27**, 95–97 (2002).
15. J. J. Duderstadt and L. J. Hamilton, *Nuclear Reactor Analysis* (Wiley, New York, 1976).
16. A. Ishimaru, *Wave Propagation and Scattering in Random Media* (Academic, New York, 1978), Vol. 1.
17. J. C. Ye, K. J. Webb, R. P. Millane, and T. J. Downar, "Modified distorted Born iterative method with an approximate Fréchet derivative for optical diffusion tomography," *J. Opt. Soc. Am. A* **16**, 1814–1826 (1999).
18. L. E. Baum and T. Petrie, "Statistical inference for probabilistic functions of finite state Markov chains," *Ann. Math. Stat.* **37**, 1554–1563 (1966).
19. S. Geman and D. McClure, "Statistical methods for tomographic image reconstruction," *Bull. Int. Stat. Inst.* **LII-4**, 5–21 (1987).
20. S. S. Saquib, C. A. Bouman, and K. Sauer, "ML parameter estimation for Markov random fields with applications to Bayesian tomography," *IEEE Trans. Image Process.* **7**, 1029–1044 (1998).
21. A. Mohammad-Djafari, "On the estimation of hyperparameters in Bayesian approach of solving inverse problems," in *Proceedings of IEEE International Conference on Acoustics, Speech, and Signal Processing* (Institute of Electrical and Electronics Engineers, New York, 1993), pp. 495–498.
22. A. Mohammad-Djafari, "Joint estimation of parameters and hyperparameters in a Bayesian approach of solving inverse problems," in *Proceedings of IEEE International Conference on Image Processing* (Institute of Electrical and Electronics Engineers, New York, 1996), Vol. II, pp. 473–476.
23. K. Lange, "An overview of Bayesian methods in image reconstruction," in *Digital Image Synthesis and Inverse Optics*, A. F. Gmitro, P. S. Idell, and I. J. LaHaie, eds., *Proc. SPIE* **1351**, 270–287 (1990).
24. C. A. Bouman and K. Sauer, "A generalized Gaussian image model for edge-preserving MAP estimation," *IEEE Trans. Image Process.* **2**, 296–310 (1993).
25. S. R. Arridge, "Photon-measurement density functions. Part 1. Analytical forms," *Appl. Opt.* **34**, 7395–7409 (1995).
26. J. S. Reynolds, A. Przdka, S. Yeung, and K. J. Webb, "Optical diffusion imaging: a comparative numerical and experimental study," *Appl. Opt.* **35**, 3671–3679 (1996).